











Properties of a Fading AGN from SDSS-IV MaNGA

Hao Mo ^{1,2,3}, Yan-Mei Chen ^{1,2,3}★, Zhi-Yun Zhang ^{1,2,3}, Alexei Moiseev ^{4,5}, Dmitry Bizyaev ^{5,6},
Yong Shi ^{1,2,3}, Qiu-Sheng Gu ^{1,2,3}, Min Bao ^{1,2,3}, Xiao Cao ^{1,2,3} and Song-Lin Li ^{7,8}

¹*School of Astronomy and Space Science, Nanjing University, Nanjing 210093, China*

²*Key Laboratory of Modern Astronomy and Astrophysics (Nanjing University), Ministry of Education, Nanjing 210093, China*

³*Collaborative Innovation Center of Modern Astronomy and Space Exploration, Nanjing 210093, China*

⁴*Special Astrophysical Observatory, Russian Academy of Sciences, Nizhny Arkhyz, Russia.*

⁵*Sternberg Astronomical Institute, Lomonosov Moscow State University, Moscow, Russia.*

⁶*Apache Point Observatory and New Mexico State University, Sunspot, NM, USA.*

⁷*Research School of Astronomy and Astrophysics, Australian National University, Canberra, ACT 2611, Australia.*

⁸*ARC Centre of Excellence for All-Sky Astrophysics in 3 Dimensions (ASTRO 3D), Australia.*

Accepted XXX. Received YYY; in original form ZZZ

ABSTRACT

We identify a fading AGN SDSS J220141.64+115124.3 from the internal Product Launch-11 (MPL-11) in Mapping Nearby Galaxies at Apache Point Observatory (MaNGA) survey. The central region with a projected radius of ~ 2.4 kpc is characterized as LINER-like line ratios while the outskirts extended to ~ 15 kpc show Seyfert-like line ratios. The [O III] $\lambda 5007$ luminosity of the Seyfert regions is a factor of 37 (2) higher than the LINER regions without (with) dust attenuation correction, suggesting that the AGN activity decreases at least $\sim 8 \times 10^3$ yrs (~ 2.4 kpc/light-speed) ago. We model the emission line spectra in the central region with double Gaussian components (a narrow core and a broad wing) and analyze the properties of each component. The narrow core component mostly co-rotates with the stellar disc, whereas the broad wing component with a median of the velocity dispersion ~ 300 km s⁻¹ is related to a wind outflow. The kinematic position angle (PA) of the ionized gas shows a $\sim 20^\circ$ twist from the galaxy center to 1.5 effective radius. The median of the PA difference between the gas and stellar components is as large as $\sim 50^\circ$ within 0.4 effective radius. The tidal feature in DESI image and star-gas misalignment suggest this galaxy is a merger remnant. Combining all these observational results as well as public available X-ray and MIR luminosities, we confirm this is a fading AGN, the merger process kick-started the central engine to quasar phase which ionized gas composed of tidal debris, and now the activity of the central black hole decreases. The discontinuity in [O III] $\lambda 5007$ flux and EQW maps is due to multiple AGN outbursts triggered by merger remnant gas inflows.

Key words: galaxies: active – galaxies: nuclei - galaxies: evolution - galaxies: individual: SDSS J220141.64+115124.3.

1 INTRODUCTION

Active galactic nuclei (AGN) can have a strong influence on the interstellar medium of the host galaxies, through photoionization of the gas, the mechanical input from radio jets or winds driven by AGNs (Morganti 2017). These kinds of AGN feedback is thought to play a critical role in regulating the evolution of both the host galaxy and the central supermassive black hole (SMBH) (e.g., Gebhardt et al. 2000; Kormendy & Ho 2013).

The AGN can photoionize gas out to a scale of ~ 1 kpc, which is the well-known narrow-line region (NLR). Observations also show that AGN-ionized gas can often extend well beyond this limit and reach tens of kiloparsecs (e.g., Liu et al. 2013; Harrison et al. 2014; Finlez et al. 2022). Extended emission line regions (EELRs) can exhibit complex morphologies and be spatially and kinematically distinct from the NLR. In early studies, the EELRs are connected with the presence of radio jets (Stockton et al. 2006). However, following works find EELRs in active galaxies without radio emission

(Husemann et al. 2013). There are some EELRs show modest electron temperatures and narrow line widths which are much smaller than that generated from direct interaction with either an outflow or a radio jet, indicating they are ionized by radiation from the nucleus (e.g., Knese et al. 2020). Due to their physical extension, EELRs provide an ideal laboratory to probe the effect of the AGN on their galaxy (e.g., Harrison et al. 2015; Sun et al. 2017). Furthermore, we can obtain a view into the activity history of the central black holes through light-travel time to the gas clouds (Aoki et al. 1994; Finlez et al. 2022; Moiseev & Smirnova 2023).

The suggestion that EELRs can be the result of a fading AGN was originally explored in an extended, highly ionized cloud called Hanny’s Voorwerp 15–35 kpc (Keel et al. 2012a) to the south of galaxy IC 2497 (Lintott et al. 2009). It is bright in SDSS *g*-band due to unusually strong [O III] $\lambda 4959$, 5007 emission lines. The difference in the energy budget between the nucleus and the ionization requirements in Hanny’s Voorwerp indicates that the AGN faded from quasar phase to a modest Seyfert or LINER level (Keel et al. 2017). Starting with the unusual morphology and *g*, *r*, *i* colors of Hanny’s Voorwerp, similar objects were discovered from the Galaxy

★ E-mail: chenym@nju.edu.cn

Zoo (Keel et al. 2012b, 2013) and from the SDSS survey (“the green beans”, Schweizer et al. 2013). These are luminous [O III] emitting clouds with extraordinarily high equivalent widths (EQWs) of several tens angstrom. More similar cases of extended ionized gas of lower luminosity AGNs have been reported using Integral Field Unit (IFU) spectroscopy in the local universe, e.g. an off-nuclear Seyfert-like compact emission line region in spiral galaxy NGC 3621 by Menezes et al. (2016), they suggest this emission line region as a “light echo” from an active galactic nucleus which has decreased by a factor of 13~500 during the last ~230 yr; two asymmetric gas clouds have been found by Comerford et al. (2017) in SDSS J1354+1327, one ~10 kpc cone of photoionized gas to the south of the galaxy center and one ~1 kpc semi-spherical front of shocked gas to the north of the galaxy center, they suggest the two clouds as a result of different AGN accretion cycles; Xu & Wang (2022, 2023) also found EELRs due to past AGN activities in NGC 7496 & NGC 5195. Mostly targeting normal galaxies, the MaNGA survey is ideal for searching low luminosity AGN echoes, which should be much more common than the extremely luminous AGN echoes identified from the SDSS imaging data, providing critical insights into the fueling, triggering, and starving of lower level AGN activity, as well as how the maintenance-mode AGN feedback operates in low-redshift galaxies. The first attempt of this sort of search was performed by French et al. (2023) who found several EELRs related to fading AGNs in MaNGA sample of post-starburst galaxies.

SDSS J220141.64+115124.3 (hereafter SDSS J2201+1151), the galaxy studied in this work, was first considered as a fading AGN candidate in Keel et al. (2012b) along with other 18 galaxies with AGN ionized regions at projected radii > 10 kpc. They estimate a ratio of 3.4 between the ionizing luminosity of the EELRs and far-infrared (FIR) AGN luminosity, indicating the extended cloud can not be ionized by an obscured AGN in SDSS J2201+1151. The most direct interpretation is that the EELRs are ionized by AGN that has faded over the light-travel time between the ionized gas and nucleus. These results were confirmed in the study of ionization history based on HST narrow band imaging (Keel et al. 2017). The ionized gas kinematics of this galaxy was briefly considered by fitting [O III] λ 5007 emission line using a single Voigt-profile (the convolution of the Gaussian and Lorentz profiles, Moiseev & Egorov 2008) based on data from Big Telescope Alt-azimuthal (BTA) in its scanning Fabry-Perot Interferometer mode (FPI, Keel et al. 2015).

In this work, we use the MaNGA data to study the gas and stellar components in SDSS J2201+1151. The paper is organized as follows. In Section 2, we give a short introduction to the MaNGA survey, general properties of this galaxy, and method of emission line fitting. In Section 3, we analyze the detailed properties of this galaxy, including the velocity field, [S II]-BPT diagram, dust attenuation, AGN luminosity, and kinematic position angle of the gas and stellar components. We discuss the observational results in Section 4. Finally, we draw conclusions in Section 5. Throughout this paper, we use the flat Λ CDM cosmological parameters with $H_0 = 70 \text{ km s}^{-1} \text{ Mpc}^{-1}$, $\Omega_m = 0.3$, and $\Omega_\Lambda = 0.7$. All wavelengths stated are in vacuum.

2 OBSERVATIONS & DATA REDUCTION

2.1 The MaNGA survey

MaNGA is one of three core programs in the fourth-generation Sloan Digital Sky Survey (SDSS-IV, Blanton et al. 2017; Yan et al. 2016a) started on July 2014, using 2.5m Sloan Foundation Telescope at

Apache Point Observatory (Gunn et al. 2006). MaNGA employs dithered observations with 17 fiber-bundle IFUs (Law et al. 2015) with 5 sizes varying between 19 fibers and 127 fibers (or 12.5''-32.5'' diameter in the sky) to explore the detailed structure of nearby galaxies (Drory et al. 2015). Two dual-channel BOSS spectrographs (Smee et al. 2013) provide simultaneous spectral coverage over 3,600~10,300Å at a median resolution of $R \sim 2,000$. MaNGA selects "Primary" and "Secondary" samples defined by two radial coverage goals. The "Primary" sample is extended out to ~1.5 effective radius (R_e , Petrosian 50% light radius) while the "Secondary" sample is extended out to ~2.5 R_e (Yan et al. 2016b). SDSS J2201+1151 belongs to the "Primary" sample and has R_e of ~10'' in r -band. The 2'' fiber diameter corresponds to 1.2kpc spatial resolution at the redshift $z \sim 0.0298$ of this galaxy. A typical exposure time of 3 hours on-sky ensures a per-fiber r -band continuum signal-to-noise ratio (S/N) of 5 at 1.5 R_e , with much higher S/N ~100 towards the center.

The Data Reduction Pipeline (DRP, Law et al. 2016) of MaNGA provides sky-subtracted and flux-calibrated 3D spectra for each galaxy. The Data Analysis Pipeline (DAP, Westfall et al. 2019) is a survey-led software package for analyzing the spectra produced by the DRP. It has been developed since 2014 and has gone through several versions, which heavily relies on pPXF (Cappellari & Emsellem 2004) and a subset of stellar templates drawn from the MaStar library (Yan et al. 2019). DAP fits the stellar continuum in each spaxel and produces estimates of the lick indexes and measurements of 21 major nebular emission lines in the MaNGA wavelength coverage. In this work, we use the following parameters from the MaNGA DAP products drawn from the internal MaNGA Product Launch-11 (MPL-11) named "MAPS-SPX-MILESHC-MASTARSSP", including line-of-sight rotation velocity of stars (V_\star), stellar velocity dispersion (σ_\star), line-of-sight rotation velocity of ionized gas (V_{gas}), gas velocity dispersion (σ_{gas}), [O III] λ 5007 flux, [O III] λ 5007 equivalent width (EQW).

2.2 General properties of SDSS J2201+1151

Figure 1 shows the gas & stellar kinematics, as well as ionization mechanism of SDSS J2201+1151. Figure 1(a) is the SDSS g, r, i color image in which the purple hexagon marks the region covered by the MaNGA bundle. Figure 1(b) is the DESI image which is ~2 mag deeper than SDSS, the tidal feature in the bottom left of this galaxy was first discovered in the Big Telescope Alt-azimuthal (BTA) R -band image presented by Keel et al. (2015), again the purple hexagon marks the region covered by the MaNGA bundle. Figure 1(c) shows the ionized gas velocity field traced by the $H\alpha$ emission line, only spaxels with $H\alpha$ S/N larger than 3 are included.

Figure 1(d) shows the velocity field of the stellar component. Red represents moving away from us while blue represents moving toward us, and the color bars indicate the value of velocities. Figure 1(e)&(f) show the [S II]-BPT diagnostic diagram (Baldwin et al. 1981; Veilleux & Osterbrock 1987) as well as the spatial resolved BPT for spaxels with S/N larger than 3 for the four emission line ($H\beta$, [O III] λ 5007, $H\alpha$, [S II] $\lambda\lambda$ 6717,6731 doublets). The solid curve in Figure 1(e) marks the theoretical upper boundary of extreme starbursts determined by Kewley et al. (2001). The black dashed line is the division between low-ionization nuclear emission-line regions (LINERs, below) and Seyfert (above) galaxies (Kewley et al. 2006). In Figure 1(e)&(f), yellow represents the LINER region and red represents the Seyfert region. It is totally out of our expectation that the central region of this object is characterized as LINER-like line ratios while the outskirts show Seyfert-like line ratios.

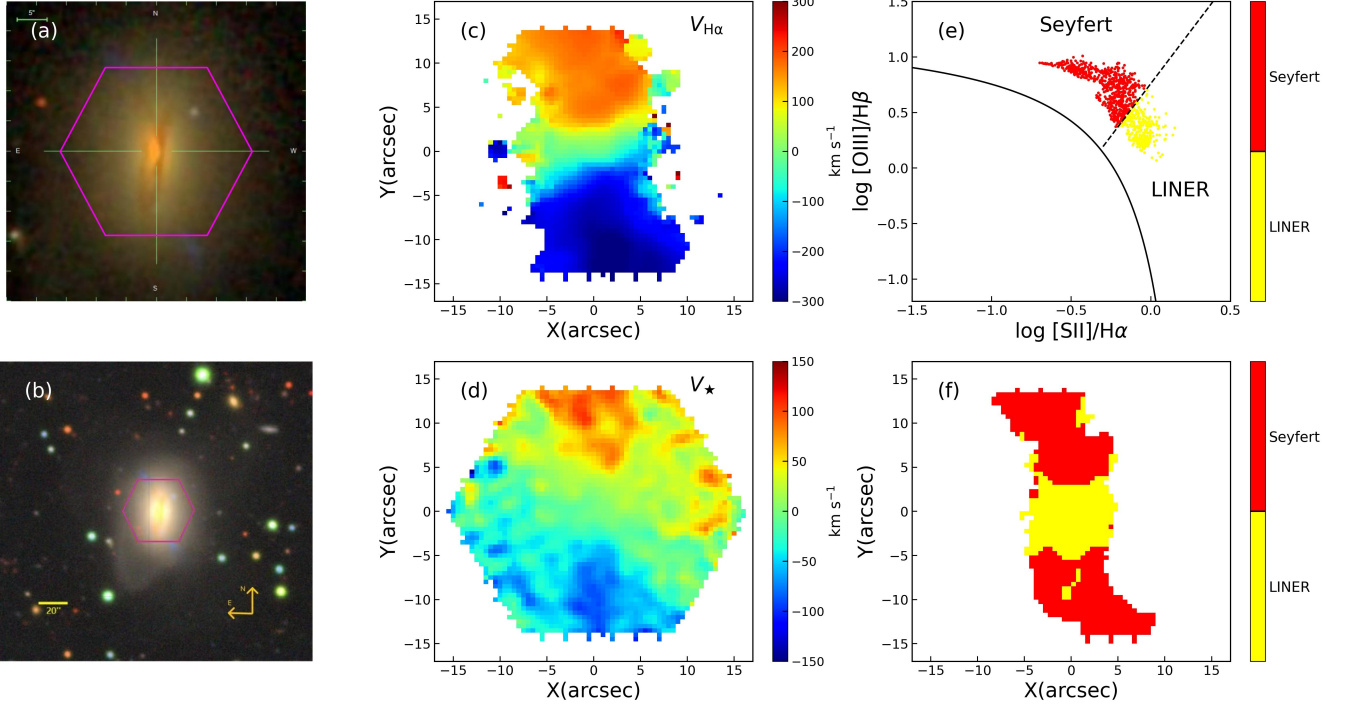


Figure 1. (a) The Sloan g, r, i color image of SDSS J2201+1151. (b) The DESI image which is ~ 2 mag deeper than SDSS. In both panel (a) and (b), the purple hexagon marks the region covered by the MaNGA bundle. (c) The ionized gas velocity field traced by $H\alpha$ emission line, only spaxels with $H\alpha$ S/N larger than 3 are included. (d) The velocity field of the stellar component. Red represents moving away from us while blue represents moving toward us, and the color bars indicate the value of velocities. (e) The [S II]-BPT diagram. The black solid curve marks the theoretical upper boundary for extreme starbursts determined by Kewley et al. (2001). The black dashed line is the division between LINER and Seyfert regions (Kewley et al. 2006). Yellow represents the LINER region and red represents the Seyfert region. (f) The spatially resolved BPT diagram. The color definition is the same as panel (e).

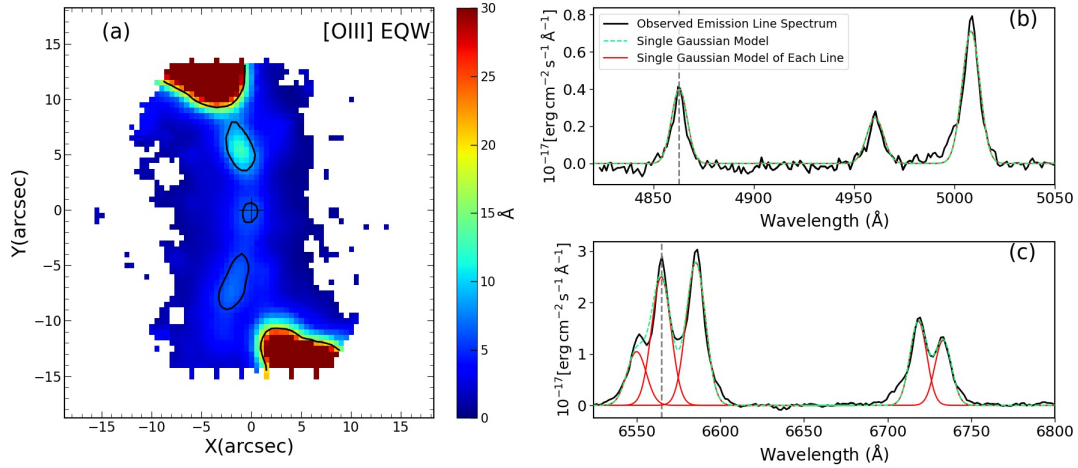


Figure 2. (a) The [O III] $\lambda 5007$ equivalent width map. The galaxy center is marked with a black cross while the black contours mark the regions with enhanced [O III] $\lambda 5007$ EQW. (b)&(c) The central emission line spectrum of the $H\beta$ & $H\alpha$ regions, respectively. Black is the observed emission line spectrum, red is the single Gaussian model of each emission line given by MaNGA DAP while green is the combination of all the Gaussian components. The vertical gray lines mark the restframe wavelength center of the $H\beta$ and $H\alpha$ emission lines.

2.3 Method of emission line fitting

In order to explore the reliability of ionization state measurements and the origin of the ionization state variations from the center to the outskirts, we check the spectrum of each spaxel, finding that in some spaxels the emission line spectra can not be modeled by a single Gaussian component, especially for the central region. Figure

2 shows the emission line spectrum for the central spaxel. Figure 2(a) shows the [O III] $\lambda 5007$ EQW map. The galaxy center is marked with a black cross while the black contours mark the regions with enhanced [O III] $\lambda 5007$ EQW. Figure 2(b)&(c) show the center emission line spectrum in the $H\beta$ and $H\alpha$ regions, respectively. Black is the observed emission line spectrum, red is the single Gaussian model

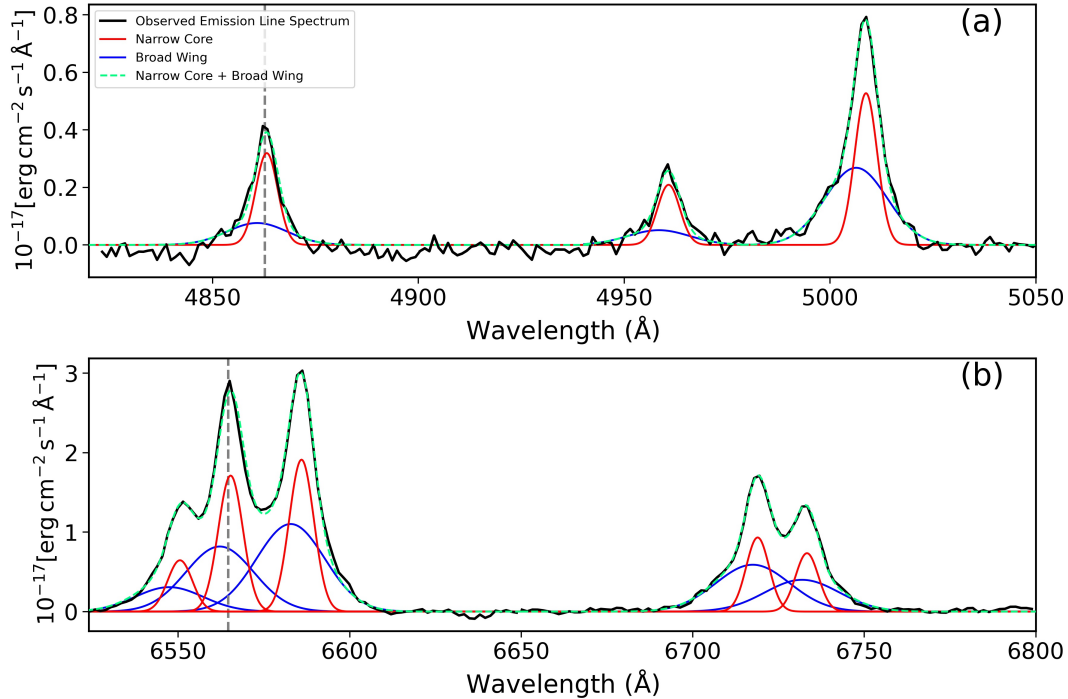


Figure 3. The central emission line spectrum of the H β (top) and H α (bottom) regions. Black is the observed emission line spectrum, red represents the narrow core component while blue represents the broad wing component. The green spectrum is the combination of the blue and red components, which is the best-fit model. The vertical gray lines mark the rest-frame wavelength center of H β and H α emission lines.

given by MaNGA DAP while green is the combination of all the Gaussian components. It is obvious that a single Gauss is insufficient for describing the profile of the emission lines.

In this section, we fit each emission line (H β , [O III] λ 4959, [O III] λ 5007, [N II] λ 6548, H α , [N II] λ 6583, [S II] λ 6717, 6731) with double Gaussian components (a narrow core plus a broad wing) using the package `curve_fit` in SciPy (Virtanen et al. 2020). Since each Gaussian component of these lines likely arises from the same physical region with similar kinematics, H β and [O III] λ 4959 are tied to have the same line center and line width as [O III] λ 5007 in the velocity space for each Gaussian component, while [N II] λ 6548, 6583 and [S II] λ 6717, 6731 are tied to have the same line center and line width as H α . We also tried to untie the line center and line width of the emission line components, finding our following results keep the same.

In Figure 3, we show the emission line spectrum of the central spaxel as well as its best-fitting double Gaussian model as an example. Black is the observed emission line spectrum, red represents the narrow core components while blue represents the broad wing components. Green is the combination of the blue and red components, which is the best-fit model. Comparing with the single Gaussian model given by MaNGA DAP in Figure 2, it is obvious that the double Gaussian describes the spectrum much better than the single Gaussian model.

In order to qualify which spaxels require double Gaussian models, we calculate the reduced chi-square (χ^2) of the single (χ_1^2) and double Gaussian models (χ_2^2) respectively. The reduced χ^2 is defined as χ^2 per degree of freedom (Lupton 1993). We apply the ratio of reduced χ^2 between single and double Gaussian models (χ_1^2/χ_2^2) to qualify how significant the fitting is improved by the double Gaussian model (Peng et al. 2014).

Figure 4(a) shows the reduced χ^2 ratio of [O III] λ 5007 region ($4980\text{\AA} \leq \lambda \leq 5030\text{\AA}$) for spaxels with [O III] λ 5007 S/N larger than 3. Figure 4(b) shows the reduced χ^2 ratio of [S II] λ 6717, 6731 region ($6690\text{\AA} \leq \lambda \leq 6760\text{\AA}$) for spaxels with [S II] λ 6717, 6731 S/N larger than 3. Spaxels with χ_1^2/χ_2^2 greater than 1.2 for both the [O III] λ 5007 and [S II] λ 6717, 6731 emission lines (the region within the black polygon) are selected for the double Gaussian fitting (Hu et al. 2008). We also visually inspect the emission line spectra by eyes to select spaxels requiring double Gaussian fitting for the emission lines. 90% spaxels selected by eyes are also selected by the ratio of reduced χ^2 method. Overall, we use the double Gaussian model (a narrow core plus a broad wing) to describe the profile of the emission line spectra for spaxels within the black polygon. For the outer regions, a single Gaussian model (narrow core) is applied to fit each emission line.

3 RESULTS

3.1 The kinematics of gas & stellar components

In this section, we study the kinematics of stellar and gas components. The stellar velocity and velocity dispersion fields are given by MaNGA DAP. The gas velocity is estimated through comparing the restframe line center of an emission line to the line center of the best-fit Gaussian model and the gas velocity dispersion is calculated from the best-fit line width. Figure 5(a) shows the stellar velocity field. Figure 5(c)&(e) show the gas velocity fields of the narrow core ($V_{\text{gas}}^{\text{NC}}$) and broad wing components ($V_{\text{gas}}^{\text{BW}}$), respectively. The narrow core component appears to co-rotate with the stellar component, while the broad wing component seems different from the stellar component and much more complicated. Figure 5(b) shows the stellar velocity dispersion, while Figure 5(d)&(f) show the gas

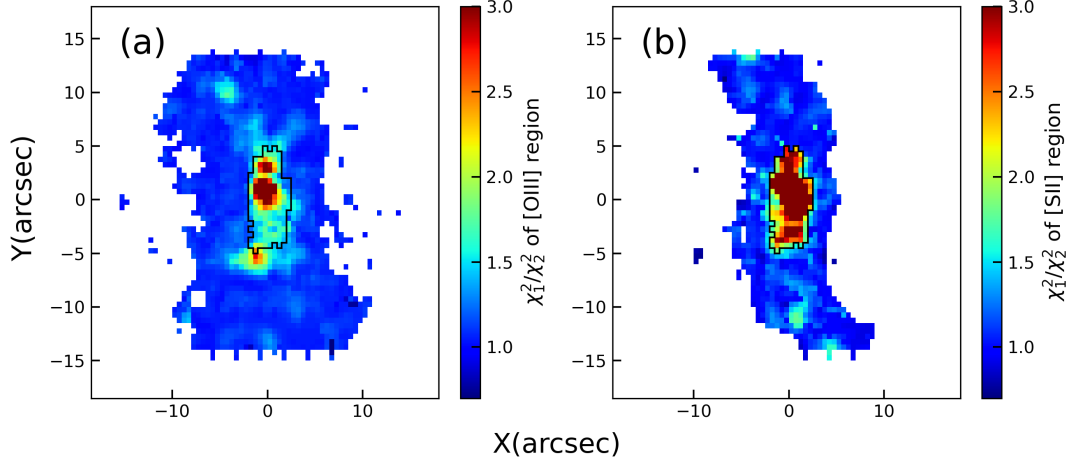


Figure 4. The ratio of χ^2 between single and double Gaussian models. (a)&(b) The reduced χ^2 ratio of the [O III] λ 5007 and [S II] $\lambda\lambda$ 6717,6731 emission line regions, respectively. Spaxels within the black polygon have reduced χ^2 ratio larger than 1.2 for both [O III] λ 5007 and [S II] $\lambda\lambda$ 6717,6731 emission lines.

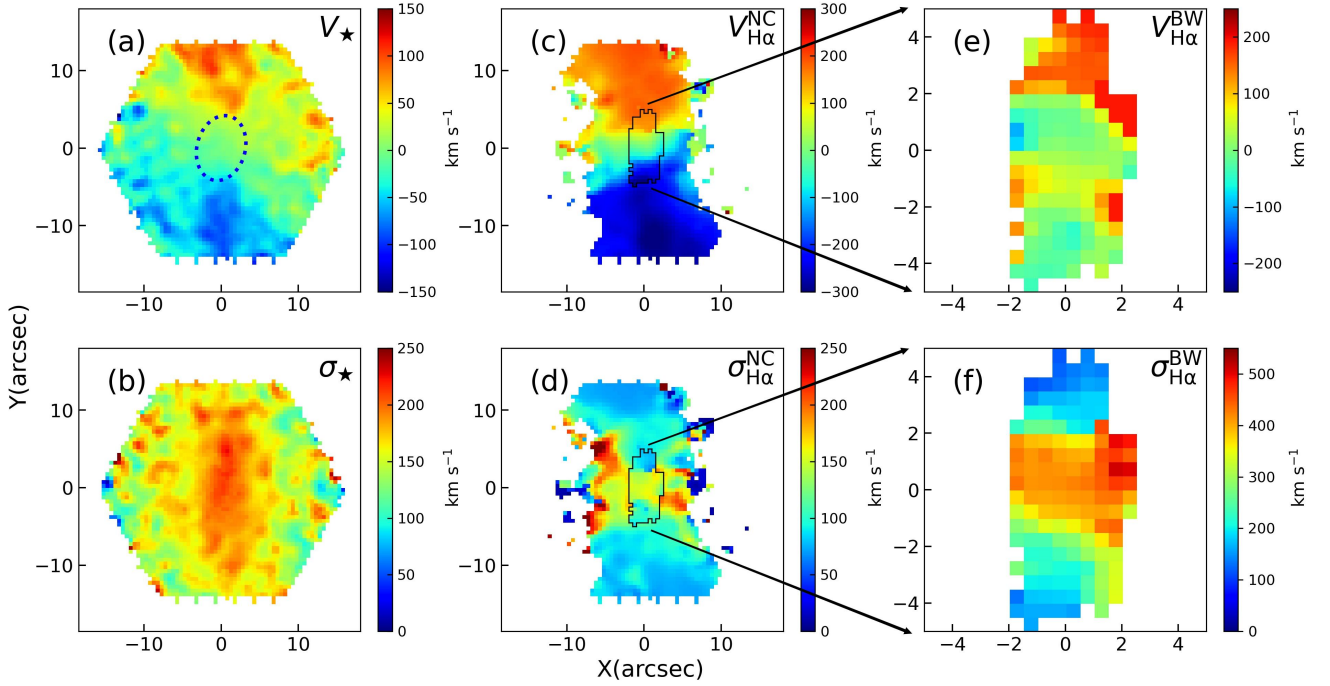


Figure 5. Kinematics for stellar and gas components. (a)&(b) The stellar velocity and velocity dispersion fields given by MaNGA DAP. (c)~(f) The gas velocity and velocity dispersion fields of the narrow core (c,d) and broad wing (e,f) components. The blue dotted ellipse in panel (a) marks $0.4R_e$ region. Similar to Figure 4, the black polygon marks the region which requires double Gaussian model.

velocity dispersion of the narrow core ($\sigma_{\text{gas}}^{\text{NC}}$) and broad wing ($\sigma_{\text{gas}}^{\text{BW}}$) components, respectively. The median of the velocity dispersion is $\sim 100 \text{ km s}^{-1}$ for the narrow core component and $\sim 300 \text{ km s}^{-1}$ for the broad wing component. The velocity dispersion of the broad wing component within the central $\pm 2''$ region is up to $400\sim 500 \text{ km s}^{-1}$, which is possibly related to a wind outflow. We discuss this possibility in more detail in Section 4.1. We note the fitting of $H\beta$ regions gives similar velocity and velocity dispersion of narrow core & broad wing components to that of $H\alpha$ region although they are not tied together in our fitting process.

3.2 The [S II]-BPT diagram

Mapping diagnostic line ratios across a galaxy reveals spatial variations in the ionization state of the gas (Rich et al. 2015; Davies et al. 2016; Florian et al. 2021). In this section, we re-visit BPT diagram using the Gaussian fitting results given in Section 2.3. Standard BPT diagnostic diagrams are based on the line ratios of [O III] λ 5007/ $H\beta$ vs. [N II] λ 6583/ $H\alpha$, [S II] $\lambda\lambda$ 6717, 6731/ $H\alpha$ or [O I] λ 6300/ $H\alpha$. In both [S II] & [O I]-BPT diagrams, high-ionization Seyfert galaxies/regions and LINERs have been shown to locate on two distinct sequences. Since the S/N of [S II] is much higher than [O I] λ 6100 in most spectra, we choose to use the [S II]-BPT diagram

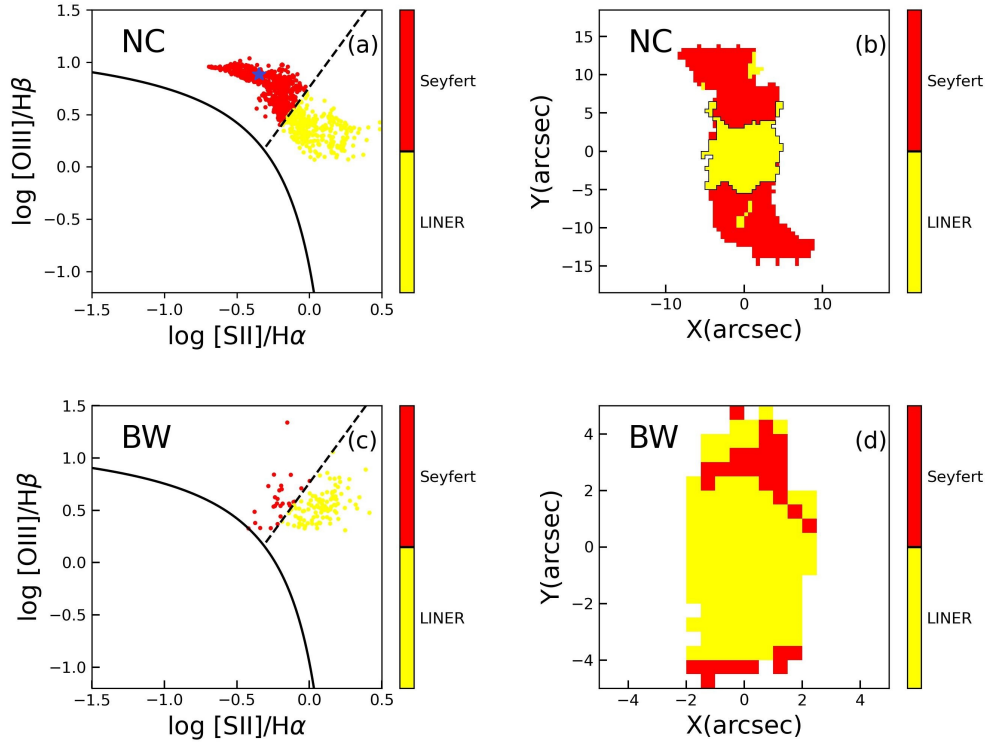


Figure 6. $[S II]/H\alpha$ vs. $[O III]/H\beta$ diagnostic diagrams. (a)&(c) The $[S II]$ -BPT diagrams of the narrow core and broad wing components, respectively. The blue star in panel (a) is the median line ratio measured from APO long-slit outside the MaNGA bundle. (b)&(d) The spatially resolved BPT diagram of the narrow core and broad wing components. The region within the black polygon is defined as LINER regions.

to separate LINER and Seyfert regions.

Figure 6 shows the $[S II]$ -BPT diagram for the narrow core (top row) and broad wing (bottom row) components. It is clear that the central region within a projected radius of $\sim 4''$ (2.4 kpc) is dominated by LINER emission not only for the narrow core but also for most of the broad wing components, while the outer region is dominated by Seyfert-like emission. This result is in agreement with what is shown in Figure 1(e) and (f). In this work, we define the region within the black polygon as LINER, see Figure 6(b).

3.3 Dust attenuation

Using the flux ratio of $H\alpha$ & $H\beta$ under Case B assumption for temperature $T \sim 10,000$ K, we correct the dust attenuation according to the following equation:

$$F_{\lambda} = F_{\lambda,0} \times 10^{-0.4k(\lambda)E(B-V)}, \quad (1)$$

where F_{λ} and $F_{\lambda,0}$ are the observed and intrinsic radiation intensity, $k(\lambda)$ is the Galactic dust extinction curve (Calzetti 2001) with $R_V = 3.1$, and color excess $E(B-V) = 0.934 \times \ln[(F_{H\alpha}/F_{H\beta})]$. The V -band extinction value in magnitudes is estimated as $A_V = E(B-V) \times R_V$ (Cardelli et al. 1989). Case B assumes that a nebula is considered optically thick to all Lyman emission lines with wavelength shorter than $Ly\alpha$, in another word these photons are absorbed and re-emitted as a combination of $Ly\alpha$ and higher order emission lines, i.e. Balmer lines (Osterbrock & Ferland 2006; Mehdipour et al. 2012; Groves et al. 2012).

Figure 7 shows the maps of $H\alpha/H\beta$ and A_V for the narrow core (top) and broad wing (bottom) components. For the narrow core component, the central LINER regions have $0.7 < A_V < 1.5$ mag

with a median value of 1.1 mag, while the Seyfert regions have $0.2 < A_V < 1.1$ mag with a median value of 0.6 mag. For the broad wing component, it has $0.6 < A_V < 2.5$ mag with a median value of 1.7 mag. The broad wing component exhibits stronger dust attenuation compared to the narrow core component, since the narrow core component traces the narrow line regions (NLRs), while the broad wing component is originated within NLRs.

3.4 AGN luminosity

In this section, we calculate the $[O III]\lambda 5007$ luminosity for the LINER and Seyfert regions according to the division in Figure 6(b). We use equation (1) for dust attenuation correction. The observed $[O III]\lambda 5007$ luminosity ($L_{[OIII]}^{obs}$) from MaNGA data is $10^{40.17}$ erg s^{-1} and $10^{40.76}$ erg s^{-1} for LINER and Seyfert regions, respectively. The $[O III]\lambda 5007$ luminosity after attenuation correction ($L_{[OIII]}^{inc}$) is $10^{41.40}$ erg s^{-1} and $10^{41.32}$ erg s^{-1} for LINER and Seyfert regions, respectively. We note that the MaNGA bundle only covers part of the two emission line nebulae with enhanced $[O III]\lambda 5007$ EQW in the northeast and southwest, which are shown as blue blobs in Figure 8(a). Thus, the $[O III]\lambda 5007$ luminosity for the Seyfert regions is underestimated.

We observe this galaxy with 3.5m telescope at the Apache Point Observatory (APO) and obtain the long-slit spectra with an observable wavelength coverage of 3874–7823 Å. Figure 8(a) shows the DESI image with the white line marking the slit position. Figure 8(b)&(c) show the ionized-gas velocities traced by $[O III]\lambda 5007$ emission line and normalized $[O III]\lambda 5007$ flux along the slit, respectively. Black dots & red crosses are measured from APO and MaNGA

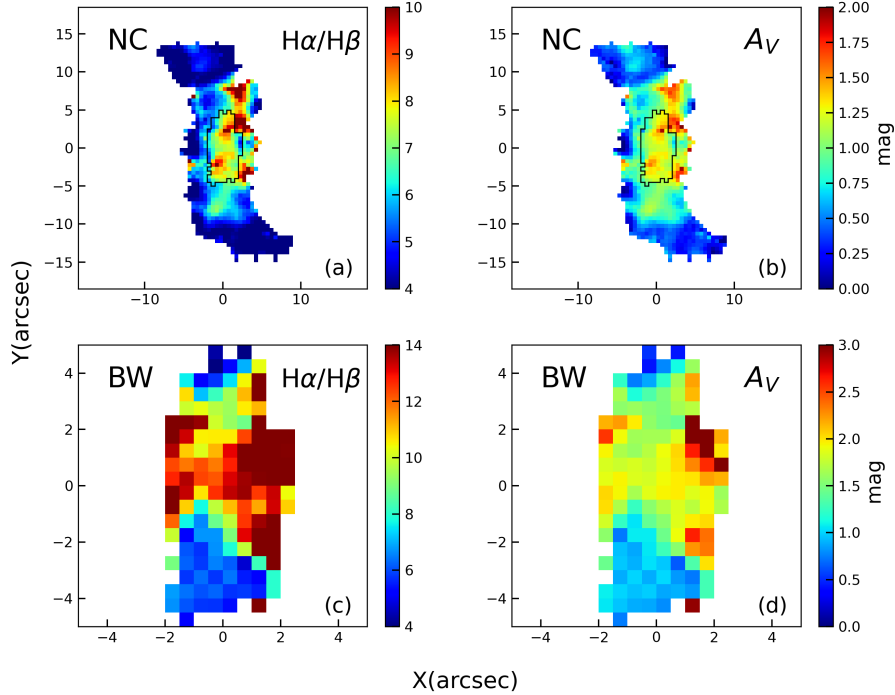


Figure 7. Maps of $H\alpha/H\beta$ and the V-band dust attenuation A_V derived from the Balmer decrement. (a)&(b) The $H\alpha/H\beta$ & A_V maps for the narrow core component. Similar to Figure 4, the black polygon marks the region which requires double Gaussian model. (c)&(d) The $H\alpha/H\beta$ & A_V maps for the broad wing component.

$\log(L_{[\text{O III}]\lambda 5007}/\text{erg s}^{-1})$	MaNGA		FPI	
	LINER	Seyfert	LINER	Seyfert
Without attenuation correction	40.17	40.76	39.70	41.27
With attenuation correction	41.40	41.32	41.36	41.71

Table 1. Logarithmic of $[\text{O III}]\lambda 5007$ luminosity measured from MaNGA and FPI. Column (2): The results are calculated from MaNGA. Column (3): The results are calculated from FPI observation. The separation between Seyfert & LINER regions is shown in Figure 6(b).

observations, respectively. The vertical blue lines mark the inner boundary of the two emission nebulae with enhanced $[\text{O III}]\lambda 5007$ flux. It is clear that APO and MaNGA observations give consistent results in both line-of-sight velocity and $[\text{O III}]\lambda 5007$ flux. The emission line ratios measured from APO data show that the two emission line nebulae outside the MaNGA bundle are also located at the Seyfert region, the median values of $\log([\text{O III}]\lambda 5007/H\beta)$ is 0.95 and $\log([\text{S II}]\lambda 6717, 6731/H\alpha)$ is -0.35 , shown as the blue star in Figure 6(a).

To obtain robust $[\text{O III}]\lambda 5007$ luminosity for the Seyfert regions, we use the $[\text{O III}]\lambda 5007$ observation from the 6m BTA in its scanning FPI mode firstly presented in Keel et al. (2015). Figure 9(a) shows the HST image which compares the continuum and emission line structure of this galaxy. Red & green are the continuum and $[\text{O III}]\lambda 5007$ emission, respectively. Figure 9(b)&(c) are the $[\text{O III}]\lambda 5007$ flux and line-of-sight velocity maps observed by FPI. The purple hexagon in Figure 9(b) marks the position of the MaNGA bundle, while pink, yellow, and red contours mark regions with enhanced $[\text{O III}]\lambda 5007$ flux at different radii. The LINER regions observed from MaNGA are marked by the black polygon. In Figure 9(c), the blue dotted ellipse shows $1R_e$ region of this galaxy and the blue dashed line marks

the kinematic major axis of the ellipse.

The observed $[\text{O III}]\lambda 5007$ luminosity measured from FPI is $10^{39.70}$ erg s $^{-1}$ and $10^{41.27}$ erg s $^{-1}$ for LINER & Seyfert regions, respectively. However, we lack the measurements of dust attenuation for the two emission line nebulae outside the MaNGA bundle. We assume that the two emission line nebula outside the MaNGA bundle have similar dust attenuation values as that measured from the long slit of APO in the Seyfert regions outside the MaNGA bundle. This gives a intrinsic luminosity of $L_{[\text{O III}]\lambda 5007}^{\text{inc}} = 10^{41.71}$ erg s $^{-1}$ for Seyfert region. In Table 1, we list the $[\text{O III}]\lambda 5007$ luminosity measured from MaNGA and FPI in detail.

The $[\text{O III}]\lambda 5007$ luminosity of the Seyfert regions is a factor of 37 (2) higher than the LINER regions without (with) dust attenuation correction, indicating the current AGN activity is insufficient to power the two emission line nebulae. One natural explanation of this discrepancy is that the AGN activity has faded with time. Given a projected distance of ~ 2.4 kpc between the nucleus and the boundary of the LINER regions defined in Figure 6(b), we suggest that the AGN activity decreases at least $\sim 8 \times 10^3$ yrs (~ 2.4 kpc/light-speed) ago.

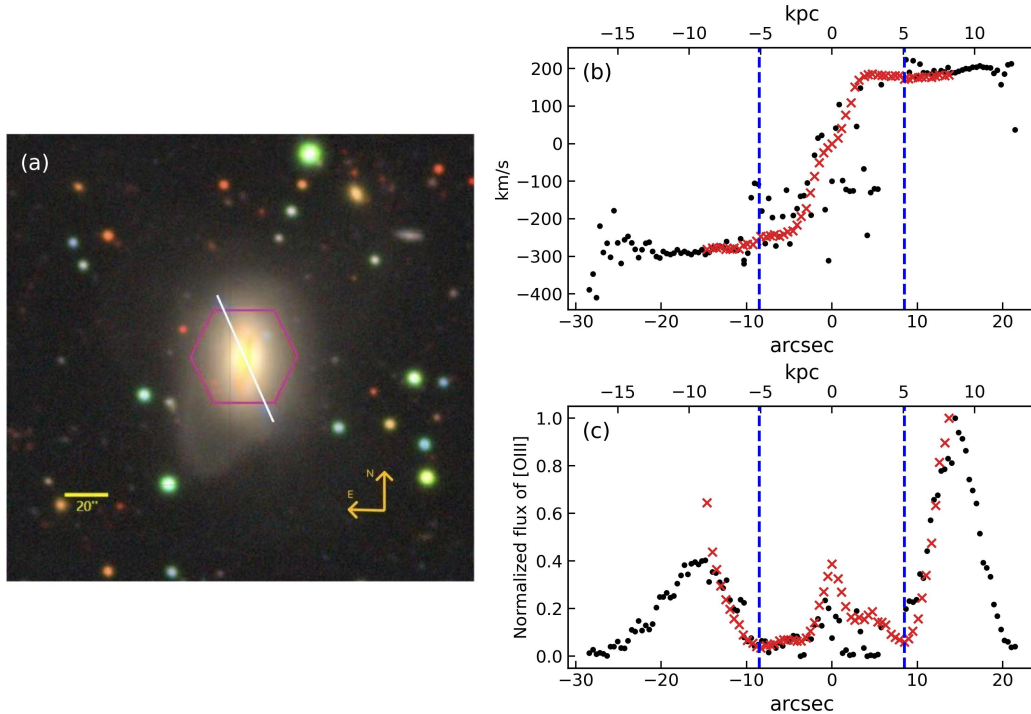


Figure 8. (a) The DESI image with the white line showing the position of the slit along the two emission line nebulae in blue. (b) The ionized-gas velocities traced by $[\text{O III}]\lambda 5007$ along the slit. (c) The normalized $[\text{O III}]\lambda 5007$ flux along the slit. Black dots & red crosses are measured from APO and MaNGA observation, respectively. The vertical blue lines mark the inner boundary of the two emission nebulae with enhanced $[\text{O III}]\lambda 5007$ flux.

3.5 Kinematic position angle of the gas and stellar components

In this section, we fit the kinematic position angle (PA) of the $[\text{O III}]\lambda 5007$ velocity field in Figure 9(c) and the stellar velocity field in Figure 5(a) as a function of radius based on the established method (Krajnović et al. 2006). The kinematic PA is defined as the counter-clockwise angle between the north and a line that bisects the velocity field of gas, measured on the approaching side. Figure 9(d) shows the kinematic PA as well as $\pm 1\sigma$ error range of the gas component as a function of radius. The PA increases from about 180° at the galaxy center to about 200° at $1.5R_e$. Figure 9(e) shows the kinematic PA as well as $\pm 1\sigma$ error range of the stellar component as a function of radius. It is clear that there is an obvious variation of stellar PA within $\sim 0.4R_e$. The ellipse with $0.4R_e$ kinematic major axis is marked in Figure 5(a). Comparing the gradients of gas & stellar PAs, we find although the warping direction of gas and stellar disks is consistent, the median of the position angle difference is as large as $\sim 50^\circ$ within $0.4R_e$, and decreases to $\sim 25^\circ$ over this radii.

4 DISCUSSION

4.1 Comparison of SDSS J2201+1151 properties with previous studies

In this section, we compare our results from Section 3 with previous studies, including kinematics of the broad wing component, AGN luminosity, and kinematics position angle of the gas component.

Based on a large sample of $\sim 39,000$ type 2 AGNs at $z < 0.3$ from the MPA-JHU Catalog of the SDSS Data Release 7 (Abazajian et al. 2009), Woo et al. (2016) perform a detailed analysis on $[\text{O III}]\lambda 5007$ emission line structure, finding that in $\sim 43.6\%$ AGNs,

the $[\text{O III}]\lambda 5007$ emission line cannot be model by a single Gaussian model. Two Gaussian components (a narrow core plus a broad wing) are required to model $[\text{O III}]\lambda 5007$ emission line, suggesting that the broad wing component originated from ionized gas outflows are prevalent among type 2 AGNs. Kang et al. (2017) suggest that strong outflows are ubiquitous in galaxies with $\sigma_{\text{H}\alpha}/\sigma_\star > 1.4$, where $\sigma_{\text{H}\alpha}$ & σ_\star is the velocity dispersion of the $\text{H}\alpha$ emission and stellar component, respectively. We closely follow the method of Kang et al. (2017) to estimate the velocity dispersion from $[\text{O III}]\lambda 5007$ profile, finding a median dispersion of $\sim 300 \text{ km s}^{-1}$ within the central $3''$ region (the aperture of a single fiber used in the early stage of SDSS survey), which is 1.5 times larger than the median of the stellar velocity dispersion $\sim 200 \text{ km s}^{-1}$ in the same region, suggesting the existence of strong outflow in galaxy SDSS J2201+1151. Moreover, the velocity dispersion of the broad wing component ranging from $400\sim 500 \text{ km s}^{-1}$ is suggested to originate from shock generated by the outflow interaction with the interstellar medium (D’Agostino et al. 2019).

Keel et al. (2012b) calculate the FIR AGN luminosity and the luminosity required for the EELRs ionization in SDSS J2201+1151, finding that the luminosity required for the EELRs ionization is 3.4 times larger than the FIR AGN luminosity, suggesting the extended cloud can not be ionized by an obscured AGN in SDSS J2201+1151. The most direct interpretation is that the EELRs are ionized by AGN that has faded over the light-travel time between the ionized gas and nucleus, which is consistent with our result that the bolometric luminosity in the LINER region is 2 times lower than the Seyfert regions.

The gas kinematic PA measured from FPI increases from about 180° at the galaxy center to about 200° at $1.5R_e$ shown in Figure 9(d). The $\sim 20^\circ$ change of PA from the inner to the outer region is consistent with Keel et al. (2015) in that they model this galaxy with

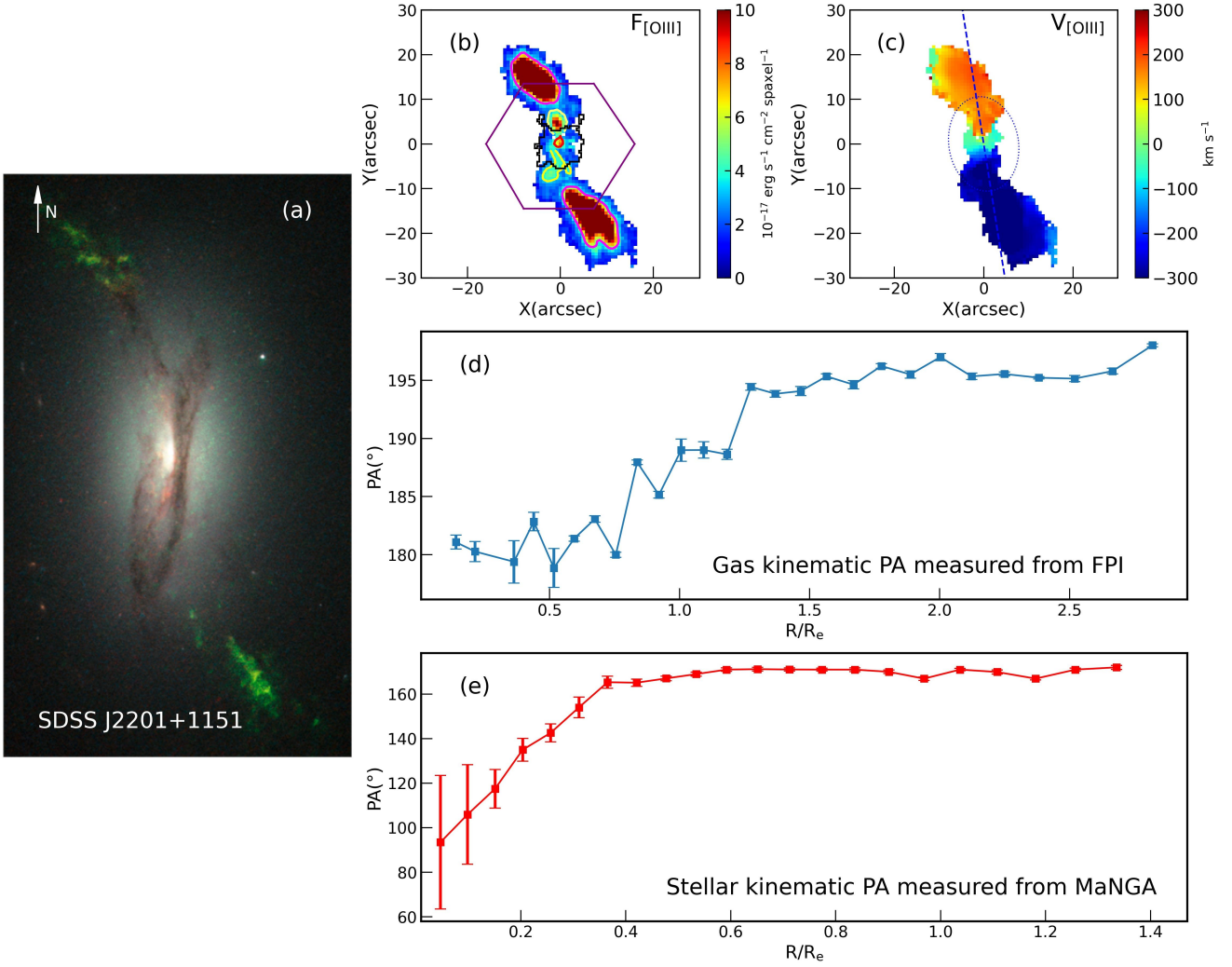


Figure 9. (a) HST image of SDSS J2201+1151 which compares the continuum and emission line structure. Red & green are the continuum and [O III] λ 5007 emission, respectively. (b) The FPI [O III] λ 5007 flux map. The purple hexagon shows the MaNGA bundle, while pink, yellow, and red contours mark the regions with enhanced [O III] λ 5007 flux. The LINER regions from MaNGA observation are marked by the black polygon. (c) The gas velocity field traced by [O III] λ 5007 emission line measured from the FPI observations. The blue dotted ellipse shows $1R_e$ region of this galaxy and the blue dashed line marks the kinematic major axis of the ellipse. (d)&(e) Kinematic position angle as a function of radius measured from the gas and stellar velocity field where the error bars show $\pm 1\sigma$ scattering region, respectively.

a differential precessing disk, finding the existence of a warped disk tilted by ~ 23 degrees to the stellar disk of the host galaxy.

4.2 SDSS J2201+1151: A fading AGN

SDSS J2201+1151 shows LINER-like ionization within its central ~ 2.4 kpc while the outskirts show Seyfert-like emission. The [O III] λ 5007 luminosity of the Seyfert region is about 2 times higher than the LINER region after dust attenuation correction, suggesting that this galaxy as a fading AGN. In this section, we further confirm this galaxy as a fading AGN by comparing its multi-band luminosities.

It is well-known that differences in the energy budget between different AGN components, like the accretion disk, dust torus, and optical ionizing regions, can be interpreted as a hint on AGN evolution (Schawinski et al. 2015; Ichikawa et al. 2019a,b; Esparza-Arredondo et al. 2020). As we know, the X-ray emission

traces the nuclear source luminosity originates from $\sim 10^{-2}$ pc-scale or timescale of 3×10^{-2} yrs (Hawkins 2007). Mid-infrared (MIR) radiation is dominated by the obscuring dust located few parsecs away from the nucleus (Ramos Almeida & Ricci 2017). [O III] λ 5007 luminosity traces the narrow emission line region which is located at kpc scale (Keel et al. 2017). The closer the structure to the galaxy center, the shorter the timescale of the evolution. In a fading scenario, we would expect the luminosity from the NLR to be higher than that from obscuring dust, while the accretion disk current bolometric luminosity being the lowest among them.

Esparza-Arredondo et al. (2020) developed a method to select fading/rising AGNs by applying the linear relations between radiations of several AGN structures at different observing bands. Figure 10(a) shows the best fit linear relation (black line) between 2-10keV X-ray luminosity and the attenuation corrected [O III] λ 5007 luminosity in logarithmic space (see their Figure 1). Figure 10(b) shows the 2-10keV X-ray luminosity versus the MIR $12\mu\text{m}$ continuum

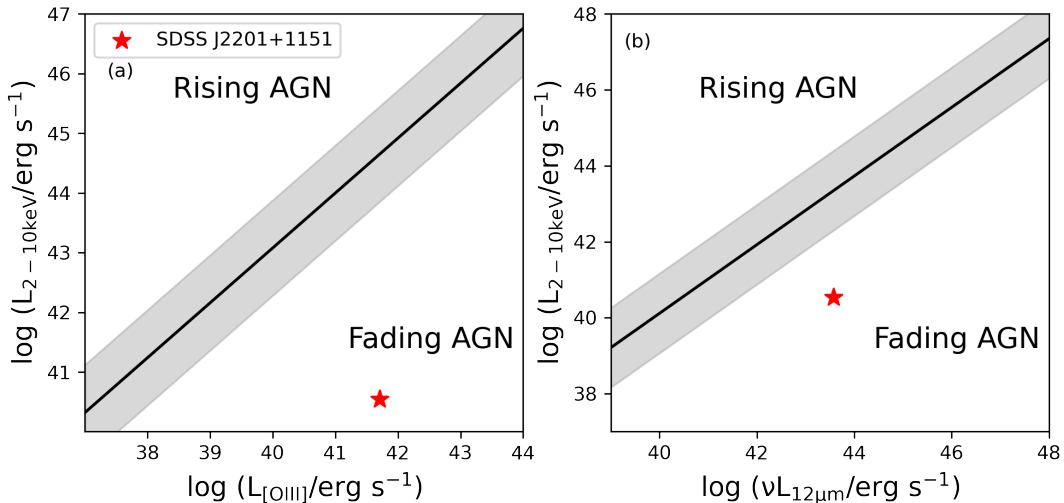


Figure 10. (a) 2–10keV X-ray luminosity versus the dust attenuation corrected $[\text{O III}]\lambda 5007$ luminosity (both in logarithmic scale). (b) 2–10keV X-ray luminosity versus the MIR $12\mu\text{m}$ continuum luminosity in logarithmic scales. The black lines show the best-fit linear with the gray shadowed region indicating the $\pm 1\sigma$ scattering region (Esparza-Arredondo et al. 2020). SDSS J2201+1151 is marked as red stars in both panels.

luminosity, again the black line is the best-fit linear relation. In both panels, the gray shadowed region indicates the $\pm 1\sigma$ scattering region. AGNs located up the $+1\sigma$ boundary are defined as rising AGNs while fading AGNs are located down the -1σ boundary. We estimate 2–10keV X-ray luminosity from XMM-Newton and MIR $12\mu\text{m}$ continuum luminosity from WISE. SDSS J2201+1151 is shown as red stars in both panels of Figure 10 and it is clear that this galaxy deviates far from the linear relation, clearly located at the fading AGN region, which is consistent with previous $[\text{O III}]\lambda 5007$ luminosity measurements of Seyfert and LINER regions in Section 3.4.

4.3 Episodic AGN outbursts

Figure 9(b) shows several regions with enhanced $[\text{O III}]\lambda 5007$ flux marked by contours with different colors, there are obvious flux gaps between these regions. The central region marked by the red contour is characterized as LINER and the outer regions marked by the pink contours are dominated by Seyfert. However, the regions in-between marked by the yellow contours on the north side is dominated by Seyfert while half of the south yellow contour is located within the LINER region. This discontinuity is also found in $[\text{O III}]\lambda 5007$ EQW map, see the black contours in Figure 2(a).

One possible explanation for the discontinuity in the distribution of $[\text{O III}]\lambda 5007$ flux and EQW is episodic AGN outbursts. The tidal feature in Figure 1(b) indicates SDSS J2201+1151 is a merger remnant. The merger process kick-started the central engine to the quasar phase which ionized gas composed of tidal debris, resulting in the regions marked by pink contours. The largest projected distance from the pink contours to the galactic center is about 15 kpc, corresponding to an AGN burst that happened at least $\sim 5 \times 10^4$ yrs (~ 15 kpc/light-speed) ago.

The regions marked by yellow contours correspond to a second AGN outburst due to the merge remnant gas inflow which occurred at least $\sim 1.3 \times 10^4$ yrs ago corresponding to a projected distance of ~ 4 kpc between the nucleus and the farthest end of the yellow contours.

5 CONCLUSIONS

We identify a fading AGN SDSS J2201+1151 from MaNGA MPL11. We use the double Gaussian model (a narrow core and a broad wing) to describe the profile of the emission line spectra for the spaxel within the black polygon marked in Figure 6(b), while only a single Gaussian model (a narrow core) is applied to fit each emission line for the outer region and analyze the detailed properties of this galaxy:

i) The central region within a projected radius of ~ 2.4 kpc is dominated by LINER emission not only for the narrow core but also for the broad wing components, while the outer region is dominated by Seyfert-like line ratios. We obtain robust $[\text{O III}]\lambda 5007$ luminosity for the Seyfert and LINER regions, finding $[\text{O III}]\lambda 5007$ luminosity of the Seyfert region is 37 (2) times higher than that of the LINER region without (with) dust attenuation correction, indicating that the AGN activity decreases at least $\sim 8 \times 10^3$ yrs ago.

ii) The narrow core component appears to be co-rotating with the stellar component, while the kinematics of the broad wing component seems different from the stellar component and much more complicated. The median velocity dispersion is ~ 100 km s^{-1} for the narrow core component and ~ 300 km s^{-1} for the broad wing component. The velocity dispersion of the broad wing component within the central $\pm 2''$ region is up to $400\sim 500$ km s^{-1} , which is related to a wind outflow. The broad wing component exhibits stronger dust attenuation compared to the narrow core component, since the narrow core component traces NLRs, while the broad wing component is originated within NLRs.

iii) There are obvious gaps between several regions with enhanced $[\text{O III}]\lambda 5007$ flux and EQW. One possible explanation for the discontinuity in the distribution of $[\text{O III}]\lambda 5007$ flux and EQW maps is episodic AGN outbursts.

iv) We use well-known linear relations between luminosities in logarithmic space of several AGN components at different wavelengths. These relations are based on the assumption that when the AGNs have no variations in luminosity, the different AGN components trace the same bolometric luminosity. Outliers of the relations imply variability in AGN activity. SDSS J2201+1151 deviates far from the linear relation, obviously located at the fading AGN region.

v) The kinematic position angle of ionized gas increases from

about 180° at the galaxy center to about 200° at $1.5R_e$ and there is an obvious variation of stellar PA within $\sim 0.4R_e$. Comparing the gradients of gas & stellar PAs, we find although the warping direction of gas and stellar disks is consistent, the median of the position angle difference is as large as $\sim 50^\circ$ within $0.4R_e$, and decreases to $\sim 25^\circ$ over this radii. The large misalignment between gas & stellar components within $0.4R_e$ suggests the influence of external process like merger on this galaxy.

The tidal features in DESI image and star-gas misalignment list above suggest this galaxy is a merger remnant. Combining all these observational results, we confirm this is a fading AGN and provide a scenario that the merger process kick-started the central engine to quasar phase which ionized gas composed of tidal debris. These episodic AGN outbursts could be the result of the galaxy merger that drives discrete accretion events onto the supermassive black hole.

ACKNOWLEDGEMENTS

M.Y.C. acknowledges support from the National Natural Science Foundation of China (NSFC grants 12333002, 11733002), the China Manned Space Project with NO. CMS-CSST-2021-A05 as well as the China Manned Space Project (the second-stage CSST science project: “Investigation of small-scale structures in galaxies and forecasting of observations”). M. B. acknowledges support from the National Natural Science Foundation of China (NSFC grants 12303009). A.M. and D.B. acknowledges partial support from the Russian Science Foundation (grant No. 22-12-00080). This research is partly based on observations obtained with the Apache Point Observatory 3.5-meter telescope, which is owned and operated by the Astrophysical Research Consortium.

Funding for the Sloan Digital Sky Survey IV has been provided by the Alfred P. Sloan Foundation, the U.S. Department of Energy Office of Science, and the Participating Institutions. SDSS-IV acknowledges support and resources from the Center for High-Performance Computing at the University of Utah. The SDSS web site is www.sdss.org.

SDSS-IV is managed by the Astrophysical Research Consortium for the Participating Institutions of the SDSS Collaboration including the Brazilian Participation Group, the Carnegie Institution for Science, Carnegie Mellon University, the Chilean Participation Group, the French Participation Group, Harvard-Smithsonian Center for Astrophysics, Instituto de Astrofísica de Canarias, The Johns Hopkins University, Kavli Institute for the Physics and Mathematics of the Universe (IPMU) / University of Tokyo, Lawrence Berkeley National Laboratory, Leibniz Institut für Astrophysik Potsdam (AIP), MaxPlanck-Institut für Astronomie (MPIA Heidelberg), Max-Planck-Institut für Astrophysik (MPA Garching), Max-Planck-Institut für Extraterrestrische Physik (MPE), National Astronomical Observatories of China, New Mexico State University, New York University, University of Notre Dame, Observatório Nacional / MCTI, The Ohio State University, Pennsylvania State University, Shanghai Astronomical Observatory, United Kingdom Participation Group, Universidad Nacional Autónoma de México, University of Arizona, University of Colorado Boulder, University of Oxford, University of Portsmouth, University of Utah, University of Virginia, University of Washington, University of Wisconsin, Vanderbilt University, and Yale University.

DATA AVAILABILITY

The data underlying this article will be shared on reasonable request to the corresponding author.

REFERENCES

- Abazajian K. N., et al., 2009, *ApJS*, **182**, 543
Aoki K., Ohtani H., Yoshida M., Kosugi G., 1994, *PASJ*, **46**, 539
Baldwin J. A., Phillips M. M., Terlevich R., 1981, *PASP*, **93**, 5
Blanton M. R., et al., 2017, *AJ*, **154**, 28
Calzetti D., 2001, *PASP*, **113**, 1449
Cappellari M., Emsellem E., 2004, *PASP*, **116**, 138
Cardelli J. A., Clayton G. C., Mathis J. S., 1989, *ApJ*, **345**, 245
Comerford J. M., Barrows R. S., Müller-Sánchez F., Nevin R., Greene J. E., Pooley D., Stern D., Harrison F. A., 2017, *ApJ*, **849**, 102
D’Agostino J. J., et al., 2019, *MNRAS*, **487**, 4153
Davies R. L., et al., 2016, *MNRAS*, **462**, 1616
Drory N., et al., 2015, *AJ*, **149**, 77
Esparza-Arredondo D., Osorio-Clavijo N., González-Martín O., Victoria-Ceballos C., Haro-Corzo S. A. R., Reyes-Amador O. U., López-Sánchez J., Pasetto A., 2020, *ApJ*, **905**, 29
Finlez C., et al., 2022, *ApJ*, **936**, 88
Florian M. K., et al., 2021, *ApJ*, **916**, 50
French K. D., Earl N., Novack A. B., Pardasani B., Pillai V. R., Tripathi A., Verrico M. E., 2023, *ApJ*, **950**, 153
Gebhardt K., et al., 2000, *ApJ*, **539**, L13
Groves B., Brinchmann J., Walcher C. J., 2012, *MNRAS*, **419**, 1402
Gunn J. E., et al., 2006, *AJ*, **131**, 2332
Harrison C. M., Alexander D. M., Mullaney J. R., Swinbank A. M., 2014, *MNRAS*, **441**, 3306
Harrison C. M., Thomson A. P., Alexander D. M., Bauer F. E., Edge A. C., Hogan M. T., Mullaney J. R., Swinbank A. M., 2015, *ApJ*, **800**, 45
Hawkins M. R. S., 2007, *A&A*, **462**, 581
Hu C., Wang J.-M., Ho L. C., Chen Y.-M., Bian W.-H., Xue S.-J., 2008, *ApJ*, **683**, L115
Husmann B., Wisotzki L., Sánchez S. F., Jahnke K., 2013, *A&A*, **549**, A43
Ichikawa K., Ueda J., Bae H.-J., Kawamuro T., Matsuoka K., Toba Y., Shidatsu M., 2019a, *ApJ*, **870**, 65
Ichikawa K., et al., 2019b, *ApJ*, **883**, L13
Kang D., Woo J.-H., Bae H.-J., 2017, *ApJ*, **845**, 131
Keel W. C., et al., 2012a, *AJ*, **144**, 66
Keel W. C., et al., 2012b, *MNRAS*, **420**, 878
Keel W. C., Manning A. M., Holwerda B. W., Mezzoprete M., Lintott C. J., Schawinski K., Gay P., Masters K. L., 2013, *PASP*, **125**, 2
Keel W. C., et al., 2015, *AJ*, **149**, 155
Keel W. C., et al., 2017, *ApJ*, **835**, 256
Kewley L. J., Dopita M. A., Sutherland R. S., Heisler C. A., Trevena J., 2001, *ApJ*, **556**, 121
Kewley L. J., Groves B., Kauffmann G., Heckman T., 2006, *MNRAS*, **372**, 961
Knese E. D., Keel W. C., Knese G., Bennert V. N., Moiseev A., Grokhovskaya A., Dodonov S. N., 2020, *MNRAS*, **496**, 1035
Kormendy J., Ho L. C., 2013, *ARA&A*, **51**, 511
Krajinović D., Cappellari M., de Zeeuw P. T., Copin Y., 2006, *MNRAS*, **366**, 787
Law D. R., et al., 2015, *AJ*, **150**, 19
Law D. R., et al., 2016, *AJ*, **152**, 83
Lintott C. J., et al., 2009, *MNRAS*, **399**, 129
Liu G., Zakamska N. L., Greene J. E., Nesvadba N. P. H., Liu X., 2013, *MNRAS*, **436**, 2576
Lupton R., 1993, *Statistics in theory and practice*
Mehdipour M., Branduardi-Raymont G., Page M. J., 2012, *A&A*, **542**, A30
Menezes R. B., Steiner J. E., da Silva P., 2016, *ApJ*, **817**, 150
Moiseev A. V., Egorov O. V., 2008, *Astrophysical Bulletin*, **63**, 181
Moiseev A. V., Smirnova A. A., 2023, *Galaxies*, **11**, 118
Morganti R., 2017, *Frontiers in Astronomy and Space Sciences*, **4**, 42

- Osterbrock D. E., Ferland G. J., 2006, *Astrophysics of gaseous nebulae and active galactic nuclei*
- Peng Z.-X., Chen Y.-M., Gu Q.-S., Zhang K., 2014, *Research in Astronomy and Astrophysics*, **14**, 913
- Ramos Almeida C., Ricci C., 2017, *Nature Astronomy*, **1**, 679
- Rich J. A., Kewley L. J., Dopita M. A., 2015, *ApJS*, **221**, 28
- Schawinski K., Koss M., Berney S., Sartori L. F., 2015, *MNRAS*, **451**, 2517
- Schweizer F., Seitzer P., Kelson D. D., Villanueva E. V., Walth G. L., 2013, *ApJ*, **773**, 148
- Smee S. A., et al., 2013, *AJ*, **146**, 32
- Stockton A., Fu H., Canalizo G., 2006, *New Astron. Rev.*, **50**, 694
- Sun A.-L., Greene J. E., Zakamska N. L., 2017, *ApJ*, **835**, 222
- Veilleux S., Osterbrock D. E., 1987, *ApJS*, **63**, 295
- Virtanen P., et al., 2020, *Nature Methods*, **17**, 261
- Westfall K. B., et al., 2019, *AJ*, **158**, 231
- Woo J.-H., Bae H.-J., Son D., Karouzos M., 2016, *ApJ*, **817**, 108
- Xu X., Wang J., 2022, *ApJ*, **933**, 110
- Xu X., Wang J., 2023, *ApJ*, **943**, 28
- Yan R., et al., 2016a, *AJ*, **151**, 8
- Yan R., et al., 2016b, *AJ*, **152**, 197
- Yan R., et al., 2019, *ApJ*, **883**, 175

This paper has been typeset from a $\text{\TeX}/\text{\LaTeX}$ file prepared by the author.